Dalton Transactions

ROYAL SOCIETY OF CHEMISTRY

PAPER

View Article Online
View Journal | View Issue

Cite this: *Dalton Trans.*, 2025, **54**, 11581

Significantly improved Curie temperature and electrical properties of Sm-doped $Pb(Ni_{1/3}Nb_{2/3})O_3$-$PbZrO_3$-$PbTiO_3$ by introducing $Pb(Mg_{1/3}Nb_{2/3})O_3$

Haoran Yu,[a] Liang Cao,[a] Jiajia Wang,[b] Jian Guo,[a] Ji Zhang [b] and Shan-Tao Zhang *[a]

Received 5th June 2025,
Accepted 7th July 2025

DOI: 10.1039/d5dt01319d

rsc.li/dalton

$Pb(Ni_{1/3}Nb_{2/3})O_3$-$PbZrO_3$-$PbTiO_3$ (PNN-PZ-PT) is one of the typical relaxor-PT piezoelectric systems. In order to further improve its Curie temperature (T_c) and piezoelectric properties, nominal $Pb(Mg_{1/3}Nb_{2/3})O_3$ (PMN) is introduced into 2mol% Sm-doped 0.36PNN-0.28PZ-0.36PT to form a (0.36 − *x*)PNN-*x*PMN-0.28PZ-0.36PT:0.02Sm (*x* = 0–0.24) quaternary solid solution. The phase, microstructure, domain structure, and electrical properties of the solid solution ceramics were investigated systematically. All the samples exhibit a single phase perovskite structure and are situated around the rhombohedral-tetragonal morphotropic phase boundary. With increasing *x*, the T_c increases gradually, while the piezoelectric coefficient d_{33} increases initially and decreases subsequently, reaching a peak value of 725 pC N^{-1} at around *x* = 0.15. In particular, this optimal composition illustrates high performance with T_c = 176 °C, planar electromechanical coupling factor k_p = 0.63, remanent polarization P_r = 30 μC cm^{-2}, and coercive field E_c = 8.9 kV cm^{-1}. This study illustrates the viability of incorporating PMN into PNN-PZ-PT to optimize the comprehensive electrical properties, potentially offering a valuable guide for developing high performance relaxor-PT materials.

1. Introduction

Piezoelectric ceramics that convert mechanical energy to electrical signals, and *vice versa*, have become indispensable in various industries. These materials are widely utilized in precise sensors, transducers, actuators, *etc.*, and thus attract tremendous long-term scientific activities.[1–5] Among the piezoelectric ceramic systems, lead zirconate titanate (PZT)-based solid solution systems have long dominated the field owing to their exceptional piezoelectric coefficients ($d_{33} \approx 500$ pC N^{-1}) and high Curie temperatures ($T_c > 300$ °C).[1,6] However, the performance optimization of traditional PZT ceramics is approaching the theoretical limits of compositional tuning, prompting researchers to explore alternative high performance piezoelectric systems. Among them, relaxor-$PbTiO_3$ (relaxor-PT) systems generally show higher piezoelectric properties, but relatively lower T_c with respect to PZT.[7–18]

Specifically, the ternary solid solutions of $Pb(Ni_{1/3}Nb_{2/3})O_3$-$PbZrO_3$-$PbTiO_3$ (PNN-PZ-PT) and $Pb(Mg_{1/3}Nb_{2/3})O_3$-$PbZrO_3$-$PbTiO_3$ (PMN-PZ-PT) are two representative examples of relaxor-PT systems and have demonstrated unique research value. For the PNN-PZ-PT ternary system, high piezoelectric properties with d_{33}–1200 pC N^{-1} have been reported by carefully controlling the composition and rare earth (RE) doping; however, the PNN-PZ-PT system possesses shortcomings of low T_c down to 105 °C. This means that in spite of its high d_{33}, the low T_c constrains the thermal stability, and thus enables wide practical applications.[7–11] In contrast, the PMN-PZ-PT ternary system maintains relatively stable electromechanical output across a broad temperature range due to its high T_c; however, the PMN-PZ-PT system shows low d_{33} as compared with its PNN-PZ-PT counterpart.[12–16] In recent years, introducing an additional component to construct multi-component solid solutions has become a key strategy for enhancing the piezoelectric performance of relaxor-PT systems; therefore, it is possible to combine the merits of PNN-PZ-PT and PMN-PZ-PT by forming a PNN-PMN-PZ-PT quaternary solid solution, aiming at further optimized or balanced electrical properties and thermal stability. It should be noted that PNN-PZ-PT ternary systems have better general properties, such as higher d_{33}, T_c and electromechanical coupling factor k_p than PNN-PT binary systems at the morphotropic phase boundary compositions.[9,12] Therefore, the ternary systems of PNN-PZ-PT

[a]*National Laboratory of Solid State Microstructures, Nanjing University, Nanjing 210023, China. E-mail: stzhang@nju.edu.cn*
[b]*School of Materials Science and Engineering, Nanjing University of Science and Technology, Nanjing 210094, China*

are chosen as the end member to construct a quaternary system of PNN-PMN-PZ-PT.

The question is how to construct an appropriate PNN-PMN-PZ-PT quaternary solid solution system. It is well-established that composition engineering near the morphotropic phase boundary (MPB) constitutes an efficient strategy for achieving superior ferroelectric and piezoelectric performance, owing to the coexistence of multiple phases enabling enhanced domain wall mobility.[1,19,20] As for the PNN-PZ-PT ternary solid solution system, a rhombohedral-tetragonal MPB occurs near 0.36PT-0.28PZ-0.36PT.[9,21] Besides, doping with rare earth elements like La^{3+} and Sm^{3+}, which replace Pb^{2+} at the perovskite A-site, has been demonstrated to enhance piezoelectricity and suppress dielectric loss by facilitating domain wall motion.[11,12,22] Based on the above description, to obtain piezoelectric ceramics with optimized or balanced electric performance, we start from a 2mol% Sm-doped 0.36PNN-0.28PZ-0.36PT ternary solid solution, and progressively introduce PMN to construct a $(0.36 - x)$PNN-xPMN-0.28PZ-0.36PT:0.02Sm (x = 0–0.24) quaternary solid solution. By synthesizing the piezoelectric ceramics, we have systematically investigated the evolution of the phase, microstructure, domain, and electrical properties as a function of composition. The optimal electrical properties are achieved at x = 0.15 with T_c of 176 °C, d_{33} of 725 pC N^{-1}, electromechanical coupling factor k_p of 0.63, remanent polarization P_r of 30 μC cm^{-2}, and coercive field E_c of 8.9 kV cm^{-1}.

2. Experimental

Sample preparation

The $(0.36 - x)$PNN-xPMN-0.28PZ-0.36PT:0.02Sm (x = 0–0.24) solid solution piezoelectric ceramics were synthesized by a two-step solid-state reaction method. In order to avoid pyrochlore phase, columbite precursors $NiNb_2O_6$ and $MgNb_2O_6$ were synthesized by weighing the dried and stoichiometric NiO/$MgCO_3$ and Nb_2O_5 powders (Sinopharm Chemical Reagent Co, ≥98%), ball milling each mixture in ethanol for 24 h, and sintering the dried mixture at 1100 °C for 4 h. Then, the obtained $NiNb_2O_6$, $MgNb_2O_6$, dried PbO (Aladdin, ≥99.9%), ZrO_2 (Aladdin, ≥99.99%), TiO_2 (Sinopharm Chemical Reagent Co, ≥99%), and Sm_2O_3 (Aladdin, ≥99.0%) powders were weighed stoichiometrically according to the chemical formula $(0.36 - x)$PNN-xPMN-0.28PZ-0.36PT:0.02Sm. The weighed powders were ball milled in ethanol for 24 h, dried at 80 °C, calcined at 850 °C for 2 h, and ball milled again for 24 h. Finally, the powders mixed with 10 wt% polyvinyl alcohol (PVA) were pressed into green disks 10 mm in diameter and ~1 mm in thickness, and sintered in covered alumina crucibles at 1200 °C for 2 h. To compensate for the volatilization of Pb at high temperature, the disks were embedded in the corresponding powders during sintering.

Characterization

The crystal structures were characterized using X-ray diffraction (XRD, Bruker D8 Advance) on ground ceramic powders. The microstructure morphologies were recorded using scanning electron microscopy (SEM, Gemini 500) on polished and thermally etched (1000 °C, 30 min) ceramics, and the grain size distribution and average grain size were estimated by using Nano Measurer software. For electrical tests, the circular surfaces of polished disks with a diameter of ~8.5 mm and thickness of ~0.5 mm were covered with a thin layer of silver paste and fired at 550 °C for 30 min. The local domain structures were investigated by piezoresponse force microscopy (PFM, MFP-3D) at a scanning frequency of 1 Hz in Vector PFM mode. The temperature-dependent dielectric constant ($\varepsilon_r - T$) and dielectric loss ($\tan\delta - T$) were measured by using an LCR meter (Agilent E4980A) on unpoled samples. The polarization–electric field (P–E) ferroelectric loops and current-electric field (J–E) curves were recorded at 1 Hz using a TF2000 analyzer (AixACCT) in silicon oil. The d_{33} was measured on poled ceramics by a Berlincourt-d_{33}-meter (ZJ-6A), and the poling was carried out at 30 kV cm^{-1} for 20 min at room temperature (~25 °C) in silicon oil. The resonant frequency f_r and anti-resonant frequency f_a were measured by an impedance analyzer (Agilent 4284) on poled ceramics. The planar electromechanical coupling factor k_p was calculated according to the following formulae:

$$\frac{1}{{k_p}^2} = 0.398\frac{f_r}{f_a - f_r} + 0.579$$

3. Results and discussion

Fig. 1(a) shows the XRD patterns of the $(0.36 - x)$PNN-xPMN-0.28PZ-0.36PT:0.02Sm ceramic powders. It can be seen that all samples exhibit a single-phase perovskite structure. Moreover, all of the ceramics exhibit nearly identical diffraction profiles with negligible shifts in the characteristic peaks, which indicates that the lattice constants of the samples remain almost unchanged upon the introduction of PMN components. This observation is reasonable and primarily attribu-

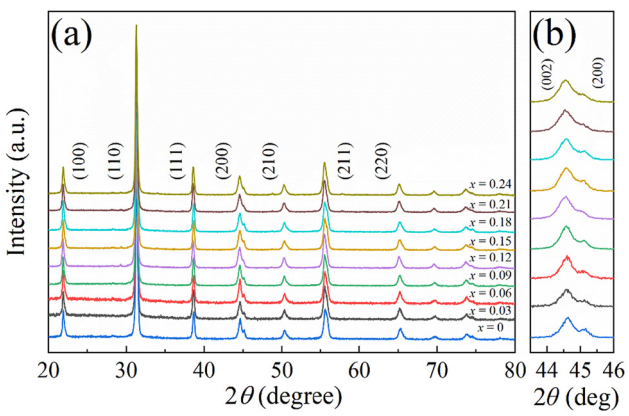

Fig. 1 (a) The XRD patterns of the $(0.36 - x)$PNN-xPMN-0.28PZ-0.36PT:0.02Sm ceramic powders (x = 0–0.24). (b) The corresponding local zoomed-in XRD around 2θ = 45°.

ted to the closely matched ionic radius of Mg^{2+} (0.72 Å) and Ni^{2+} (0.69 Å) within the perovskite lattice. Fig. 1(b) displays a local zoomed-in view of the XRD patterns around 2θ = 45°, where the split (002) and (200) diffraction peaks are clearly observable across all samples and the (200) peak exhibits markedly weaker intensity, indicating that the phase structure of all the ceramics is close to the rhombohedral-tetragonal MPB region.[7,23] Notably, the samples with x = 0.21 and x = 0.24 show a reduced intensity of the (200) diffraction peak compared with other compositions, suggesting a possible deviation from the MPB, which may correlate with the reduction in piezoelectric performance, as will be discussed below.

Fig. 2 displays the typical SEM microstructural micrographs of all ceramics after polishing and thermal etching, and the insets illustrate the corresponding grain size distributions. As can be observed from the figures, all of the ceramics possess a dense microstructure without cracks or voids. The average grain size (AGS) of each ceramic, which was calculated by counting more than 100 grains, decreases monotonously from 2.80 μm for x = 0 to 1.40 μm for x = 0.24 with the increase in x value. This phenomenon may be attributed to the inhibition of grain boundary migration during sintering by the introduction of PMN content.[24] Moreover, such a reduction in grain size will affect the macroscopic properties, as will be discussed below.

In order to better understand the impact of introducing the PMN component on the domain structure of the (0.36 − x)PNN-xPMN-0.28PZ-0.36PT:0.02Sm system, the typical PFM height, in-plane amplitude, and in-plane phase images within an area of 10 × 10 μm^2 of the x = 0 and x = 0.15 piezoelectric ceramics were comparatively investigated and are illustrated in Fig. 3. Both ceramics exhibit the emergence of large striped domains and irregular labyrinth-shaped domains, corresponding to tetragonal and rhombohedral phase structures, respectively.[8,25] This observation confirms that the samples are located near the MPB where the rhombohedral and tetragonal phases coexist, which actually aligns with the XRD patterns mentioned above. Additionally, it is seen that with the introduction of the PMN component, the domain size significantly decreases, correlating with the reduced grain size discussed above.[26,27] A smaller domain, which is usually accompanied by lower energy barriers, means a higher density of the domain wall and suggests a flattening of the Gibbs free energy profile.[28] Consequently, it is reasonable to expect that the piezoelectric performance of the x = 0.15 ceramics will show an enhancement compared with the x = 0 ceramics, which is the case, as will be shown in the following.

Fig. 4 displays the temperature-dependent dielectric constant ε_r and dielectric loss $\tan\delta$ of the (0.36 − x)PNN-xPMN-0.28PZ-0.36PT:0.02Sm ceramics. It is noteworthy that the dielectric loss at 1 kHz and 25 °C initially decreases and then increases, reaching a minimum value of 2.75% at x = 0.15. As observed from Fig. 4, all samples exhibit typical diffuse dielectric peaks. To quantitatively investigate the relaxation behavior of the piezoceramics, the relaxor degree γ is calculated *via* the modified Curie–Weiss law using the formula

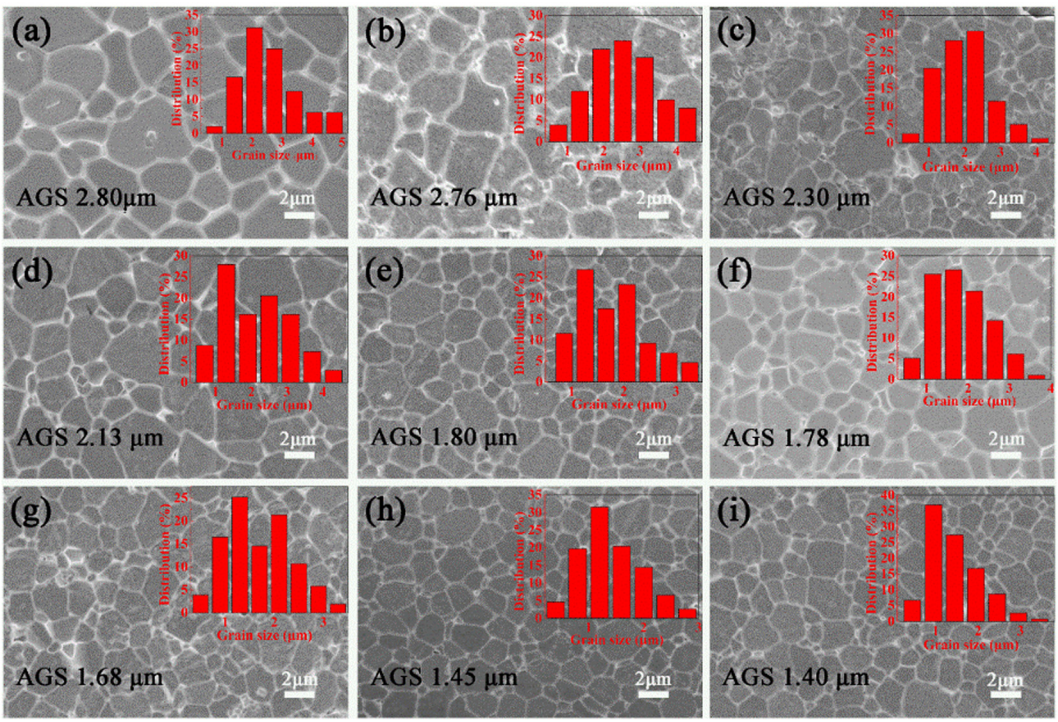

Fig. 2 The typical SEM morphologies of the (0.36 − x)PNN-xPMN-0.28PZ-0.36PT:0.02Sm ceramics: (a) x = 0, (b) x = 0.03, (c) x = 0.06, (d) x = 0.09, (e) x = 0.12, (f) x = 0.15, (g) x = 0.18, (h) x = 0.21, and (i) x = 0.24.

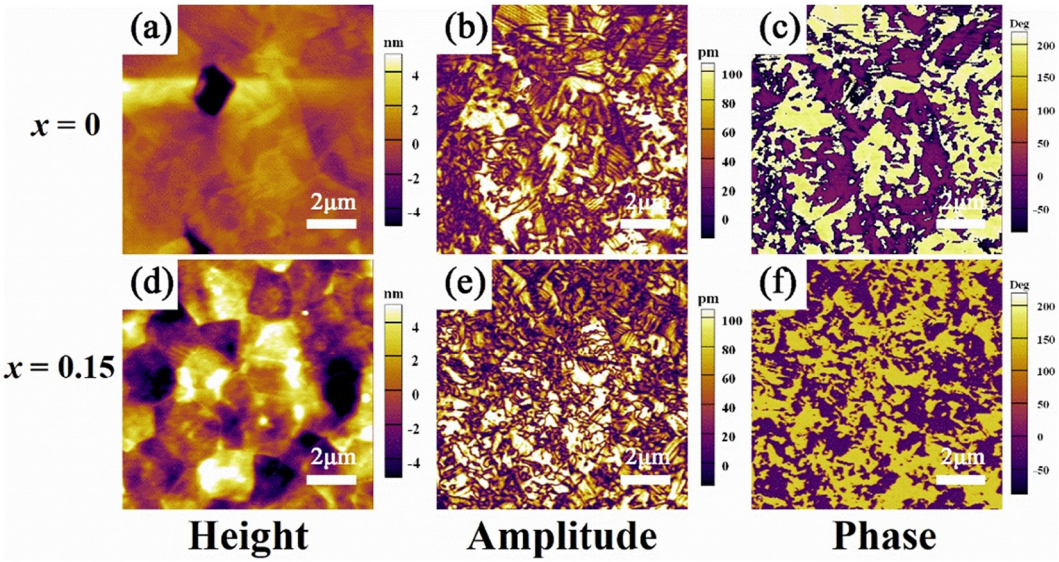

Fig. 3 The typical PFM height, in-plane amplitude, and in-plane phase images of the (0.36 − *x*)PNN-*x*PMN-0.28PZ-0.36PT:0.02Sm ceramics. (a–c) *x* = 0, (d–f) *x* = 0.15.

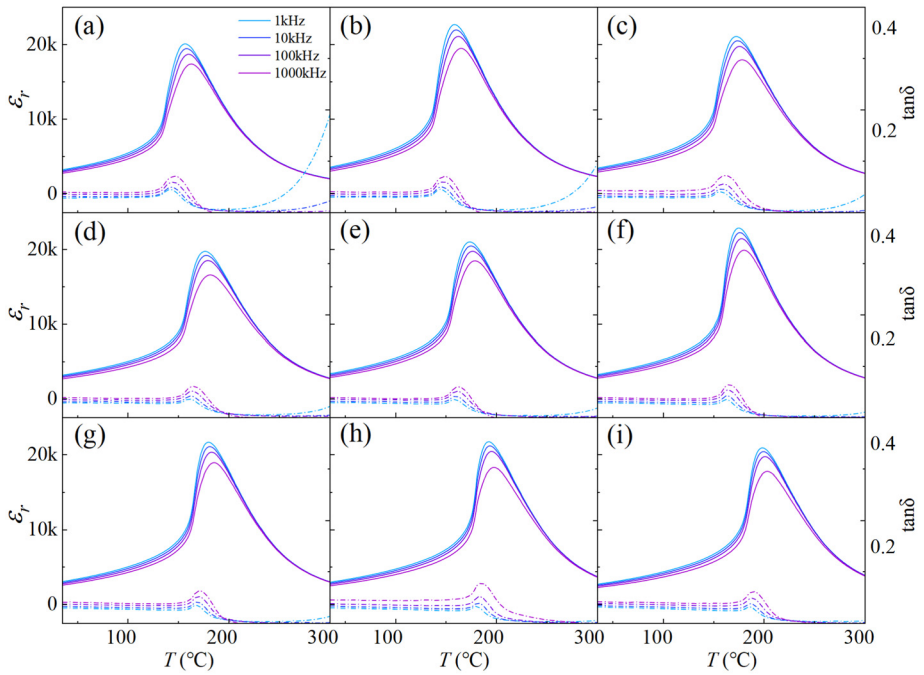

Fig. 4 The temperature-dependent ε_r and tan δ of the (0.36 − *x*)PNN-*x*PMN-0.28PZ-0.36PT:0.02Sm ceramics: (a) *x* = 0, (b) *x* = 0.03, (c) *x* = 0.06, (d) *x* = 0.09, (e) *x* = 0.12, (f) *x* = 0.15, (g) *x* = 0.18, (h) *x* = 0.21, and (i) *x* = 0.24.

$\frac{1}{\varepsilon} - \frac{1}{\varepsilon_m} = \frac{(T - T_m)^\gamma}{C}$,[29] where ε_m and T_m are the maximum dielectric constant and the corresponding temperature and ε is adopted in the range of $T > T_m$, and C is the Curie coefficient. Generally, the value of γ is between 1 and 2, and γ = 1 and γ = 2 represents the ideal normal and relaxor ferroelectrics, respectively. Fig. 5 shows the composition-dependent average grain size, T_c determined at 1 kHz, and relaxor degree γ of all the piezoceramics. One can see from Fig. 5 that the T_c of the (0.36 − *x*)PNN-*x*PMN-0.28PZ-0.36PT:0.02Sm ceramics exhibits a gradual increasing trend with increasing *x* value, ascending from 156 °C at *x* = 0 to 198 °C at *x* = 0.24. This result indicates the feasibility of achieving excellent thermal stability through PMN component regulation in PNN-PZ-PT systems. Considering that the PNN-PZ-PT ternary system demonstrates lower T_c than the PMN-PZ-PT ternary

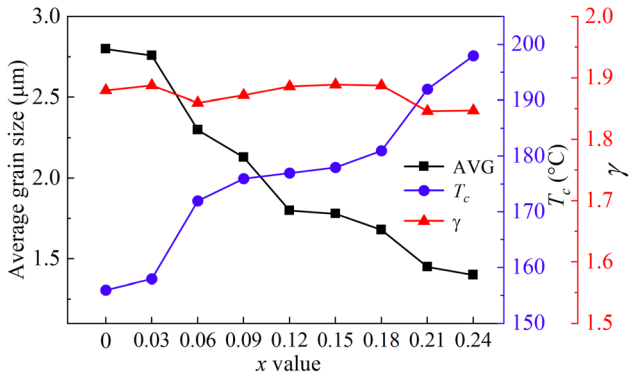

Fig. 5 The composition-dependent average grain size, T_c and relaxor degree γ of the (0.36 − x)PNN-xPMN-0.28PZ-0.36PT:0.02Sm ceramics.

system,[9,20,30] it is reasonable that the gradual substitution of PNN with PMN enhances the PNN-PMN-PZ-PT quaternary system's Curie temperature. Meanwhile, as the x value increases, the average grain size gradually decreases, which is completely opposite to the increasing trend of Curie temperature. Besides, the relaxor degree γ of all samples remains a high value but within a narrow range between 1.8 and 1.9, indicating that all the prepared piezoceramics are relaxor ferroelectrics. Piezoelectric ceramics with high relaxor degree exhibit relatively larger d_{33} and slender P–E hysteresis loops due to the response of numerous highly responsive polar nanoregions (PNRs). As shown in Fig. 5, the relaxor degree shows a maximum value at x = 0.15 with γ = 1.89, where the maximum piezoelectric coefficient is probably achieved. This result aligns with the piezoelectric properties presented below.

The room temperature ferroelectric P–E loops and J–E curves of the (0.36 − x)PNN-xPMN-0.28PZ-0.36PT:0.02Sm piezoelectric ceramics measured at 30 kV cm^{-1} are plotted in Fig. 6(a)–(i). It can be observed that all of the ceramics exhibit a saturated slender P–E loop and double peak J–E curve, indicating that all the ceramics possess ferroelectric nature. To more intuitively characterize the compositional dependence of ferroelectricity, Fig. 7 shows the maximum polarization P_m, remanent polarization P_r and coercive electric field E_c as a function of x value. One can see that the E_c monotonically increases with rising x value, from 8.1 kV cm^{-1} at x = 0 to 9.6 kV cm^{-1} at x = 0.24, which is primarily attributed to the gradual reduction in grain size, as shown in Fig. 2, which leads to higher grain boundary density that hinders domain wall motion.[31] Notably, the E_c remains nearly unchanged at x = 0.12 and x = 0.15, consistent with the stable grain size observed in Fig. 2(e and f). In addition, both P_m and P_r initially increase and then decrease with increasing x value, reaching peak values of P_m = 40.8 μC cm^{-2} and P_r = 31.5 μC cm^{-2} at x = 0.12. However, at x = 0.21, the P_m and P_r unexpectedly show a slight increase instead of a continuous decrease. This anomaly may be attributed to the fact that the composition begins to deviate from the MPB region and shifts toward a rhombohedral phase structure, as indicated by the XRD shown in Fig. 1. While the rhombohedral phase has eight possible polarization directions, compared to six directions in the tetragonal phase, the

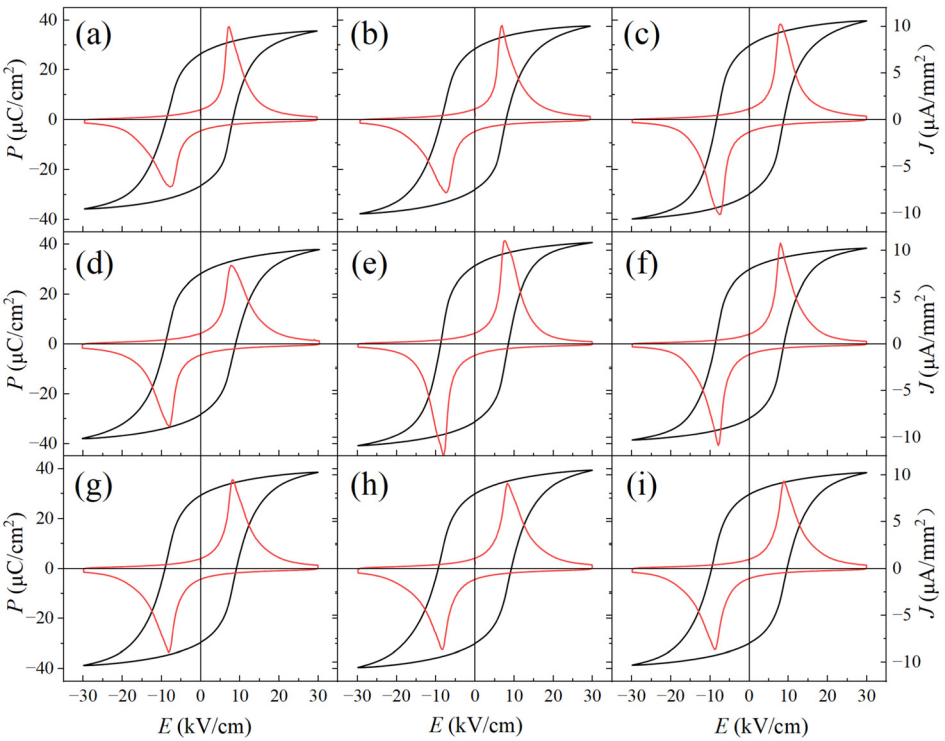

Fig. 6 The P–E loops of the (0.36 − x)PNN-xPMN-0.28PZ-0.36PT:0.02Sm ceramics: (a) x = 0, (b) x = 0.03, (c) x = 0.06, (d) x = 0.09, (e) x = 0.12, (f) x = 0.15, (g) x = 0.18, (h) x = 0.21, and (i) x = 0.24.

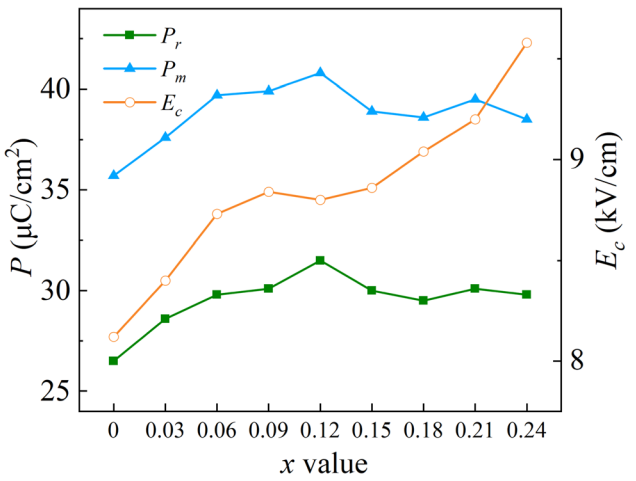

Fig. 7 The composition-dependent P_r, P_m and E_c of the (0.36 − x)PNN-xPMN-0.28PZ-0.36PT:0.02Sm ceramics.

deviation from MPB to the rhombohedral phase structure may enhance the density of switchable dipoles, thus leading to an increase in the P_m and P_r values.[32]

Fig. 8 shows the composition-dependent d_{33} and k_p of the (0.36 − x)PNN-xPMN-0.28PZ-0.36PT:0.02Sm ceramics measured at room temperature. With increasing x value, the d_{33} first increases and then decreases, reaching a peak value of d_{33} = 725 pC N^{-1} at x = 0.15. This increase of d_{33} at first is attributed to the introduction of the PMN into the PNN-PZT system inducing a reduction in grain size and thus an increase in domain wall density. However, when the PMN component further increases, the contribution from grain size reduction reaches a threshold, and at the same time, the phase of the ceramics tends to deviate from the MPB region toward the rhombohedral side at x = 0.21, leading to a decline in piezoelectric performance. These results are consistent with the above phase and ferroelectric property analyses. Additionally, the k_p exhibits a gradual rising trend with increasing x, but the k_p value is limited in a very narrow range of 0.60–0.64. In general, the optimal piezoelectric property with d_{33} = 725 pC N^{-1} and k_p = 0.63 is achieved at x = 0.15, better than the previously reported similar composition of 0.36PNN-0.24PZ-0.40PT piezoceramic with d_{33} = 545 pC N^{-1} and k_p = 0.54.[9]

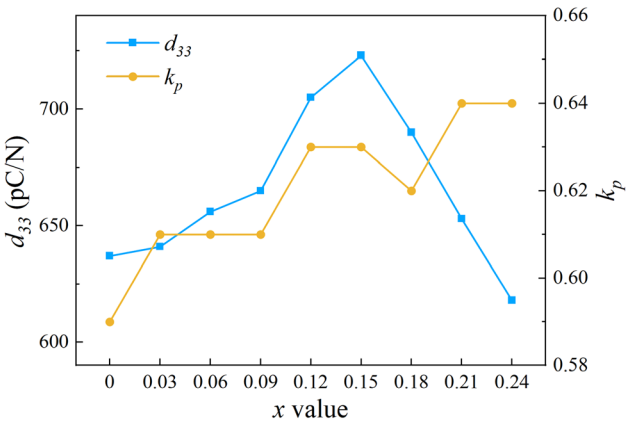

Fig. 8 The room temperature d_{33} and k_p of the (0.36 − x)PNN-xPMN-0.28PZ-0.36PT:0.02Sm ceramics.

4. Conclusions

In this work, (0.36 − x)PNN-xPMN-0.28PZ-0.36PT:0.02Sm (x = 0–0.24) piezoelectric ceramics were synthesized and the phase, microstructure, domain, and electric properties of the ceramics systematically investigated. The results reveal that with the gradual introduction of PMN, the Curie temperature progressively increases, while the electrical performance initially improves and then declines. The composition with x = 0.15 exhibits the optimal electrical property with T_c = 176 °C, d_{33} = 725 pC N^{-1}, k_p = 0.63 P_r = 30 μC cm^{-2}, and E_c = 8.9 kV cm^{-1}. This work provides an insight into constructing the PNN-PMN-PZ-PT quaternary solid solution system with improved comprehensive electrical properties, offering guidance for further designing high-performance piezoelectric materials.

Author contributions

Haoran Yu: sample preparation, data curation, formal analysis. Liang Cao: data curation, formal analysis. Jiajia Wang: data curation and validation. Jian Guo: data curation, formal analysis. Ji Zhang: wirting – original draft. Shan-Tao Zhang: funding acquisition, writing – reviewing & editing.

Conflicts of interest

The authors declare that they have no competing financial interests.

Data availability

The data that support the findings of this study are available from the corresponding authors upon reasonable request.

Acknowledgements

This work was supported by the National Key R&D Program of China (2020YFA0711504), the National Natural Science Foundation of China (12374084), and the Dengfeng B project of Nanjing University.

References

1 G. H. Haertling, *J. Am. Ceram. Soc.*, 1999, **82**, 797–818.
2 Y. Saito, H. Takao, T. Tani, T. Nonoyama, K. Takatori, T. Homma, T. Nagaya and M. Nakamura, *Nature*, 2004, **432**, 84–87.
3 S. Trolier-McKinstry, S. J. Zhang, A. J. Bell and X. L. Tan, *Annu. Rev. Mater. Res.*, 2018, **48**, 191–217.

4 W. F. Bai, P. Zheng, F. Wen, J. Zhang, D. Chen, J. W. Zhai and Z. G. Ji, *Dalton Trans.*, 2017, **46**, 15340–15353.
5 Y. J. Shi, H. R. Bai, F. Yan, R. Hu, K. K. Chen, B. Shen and J. W. Zhai, *Dalton Trans.*, 2020, **49**, 5573–5580.
6 X. Y. Tang, Z. M. Hu, V. Koval, H. Baxter, M. Eriksson, R. Whiteley, K. Banerjee, G. Viola, B. Yang and H. X. Yan, *J. Materiomics.*, 2025, **11**, 101052.
7 L. Bian, Q. Wang, X. D. Qi, K. Li, S. He, G. C. Jiang, Y. L. Yang and B. Yang, *Ceram. Int.*, 2024, **50**, 5739–5745.
8 L. Bian, X. D. Qi, K. Li, J. H. Fan, Z. M. Li, E. W. Sun, B. Yang, S. X. Dong and W. W. Cao, *J. Eur. Ceram. Soc.*, 2021, **41**, 6983–6990.
9 Q. Wang, L. Bian, S. He, N. Wang, B. Yang and W. W. Cao, *J. Alloys Compd.*, 2024, **1002**, 175249.
10 W. Peng, J. L. Chang, J. W. Zhao, D. W. Wang, Z. Liu, G. S. Wang and S. X. Dong, *J. Materiomics*, 2024, **10**, 995–1003.
11 G. G. Peng, D. Y. Zheng, C. Cheng, J. Zhang and H. Zhang, *J. Alloys Compd.*, 2017, **693**, 1250–1256.
12 J. Guo, M. Y. Yuan, H. R. Yu, J. Zhang, G. L. Yuan and S. T. Zhang, *Dalton Trans.*, 2024, **53**, 16054–16065.
13 P. B. Wang, Q. H. Guo, F. Li, F. Q. Xia, H. Hao, H. J. Sun, H. X. Liu and S. J. Zhang, *J. Am. Ceram. Soc.*, 2021, **104**, 5127–5137.
14 Q. H. Guo, X. Y. Meng, F. Li, F. Q. Xia, P. B. Wang, X. Y. Gao, J. S. Wu, H. J. Sun, H. Hao, H. X. Liu and S. J. Zhang, *Acta Mater.*, 2021, **211**, 116781.
15 L. Wang, R. H. Liang, C. L. Mao, M. Gao, G. Du, F. Cao, G. S. Wang and X. L. Dong, *J. Am. Ceram. Soc.*, 2012, **95**, 445–448.
16 Q. H. Guo, F. Li, F. Q. Xia, X. Y. Gao, P. B. Wang, H. Hao, H. J. Sun, H. X. Liu and S. J. Zhang, *ACS Appl. Mater. Interfaces*, 2019, **11**, 43359–43367.
17 H. W. Shi, F. Li, W. Liu, C. Liang, X. L. Ji, M. S. Long, W. P. Gong, C. C. Wang and L. Shan, *J. Phys. D: Appl. Phys.*, 2022, **55**, 185301.
18 X. Y. Lin, J. N. Ding, X. H. Li, Z. Tang, H. B. Chen, H. Dong, A. H. Wu and L. W. Jiang, *Dalton Trans.*, 2023, **52**, 14917–14927.
19 J. Rödel, W. Jo, K. T. P. Seifert, E. M. Anton, T. Granzow and D. Damjanovic, *J. Am. Ceram. Soc.*, 2009, **92**, 1153–1177.
20 T. R. Shrout and S. J. Zhang, *J. Electroceram.*, 2007, **19**, 113–126.
21 L. Bian, X. D. Qi, K. Li, Y. Yu, L. J. Liu, Y. F. Chang, W. W. Cao and S. X. Dong, *Adv. Funct. Mater.*, 2020, **30**, 2001846.
22 Z. Li, H. C. Thong, Y. F. Zhang, Z. Xu, Z. Zhou, Y. X. Liu, Y. Y. S. Cheng, S. H. Wang, C. L. Zhao, F. Chen, K. Bi, B. Han and K. Wang, *Adv. Funct. Mater.*, 2020, **31**, 2005012.
23 Q. Wang, L. Bian, K. Li, Y. C. Liu, Y. L. Yang, B. Yang and W. W. Cao, *J. Mater. Sci. Technol.*, 2024, **175**, 258–265.
24 G. Bernard-Granger and C. Guizard, *Acta Mater.*, 2008, **56**, 6273–6282.
25 X. D. Qi, Y. Zhao, E. W. Sun, J. Du, K. Li, Y. Sun, B. Yang, R. Zhang and W. W. Cao, *J. Eur. Ceram. Soc.*, 2019, **39**, 4060–4069.
26 W. W. Cao and C. A. Randall, *J. Phys. Chem. Solids*, 1996, **57**, 1499–1505.
27 C. A. Randall, N. Kim, J. P. Kucera, W. W. Cao and T. R. Shrout, *J. Am. Ceram. Soc.*, 1998, **81**, 677–688.
28 L. Chen, H. Liu, H. Qi and J. Chen, *Prog. Mater. Sci.*, 2022, **127**, 100944.
29 J. Li, F. Li, Z. Xu and S. Zhang, *Adv. Mater.*, 2018, **32**, 1802155.
30 V. Koval, C. Alemany, J. Briančin, H. Brunckova and K. Saksl, *J. Eur. Ceram. Soc.*, 2003, **23**, 1157–1166.
31 J. Schulthei, G. Picht, J. Wang, Y. A. Genenko, L. Q. Chen, J. E. Daniels and J. Koruza, *Prog. Mater. Sci.*, 2023, **136**, 101101.
32 F. Li, S. J. Zhang, Z. Xu, X. Y. Wei, J. Luo and T. R. Shrout, *J. Appl. Phys.*, 2010, **108**, 034106.